1-2019

First MMS Observation of Energetic Particles Trapped in High-Latitude Magnetic Field Depressions

Katariina Nykyri
Embry-Riddle Aeronautical University, nykyrik@erau.edu

Christina Chu
Embry-Riddle Aeronautical University

Xuanye Ma
Embry-Riddle Aeronautical University, max@erau.edu

Stephen A. Fuselier
South West Research Institute

Rachel Rice
Embry-Riddle Aeronautical University

Scholarly Commons Citation

Nykyri, K., Chu, C., Ma, X., Fuselier, S. A., & Rice, R. (2019). First MMS Observation of Energetic Particles Trapped in High-Latitude Magnetic Field Depressions. *Journal of Geophysical Research: Space Physics, 124*(1). https://doi.org/10.1029/2018JA026131

JGR Space Physics

RESEARCH ARTICLE
10.1029/2018JA026131

First MMS Observation of Energetic Particles Trapped in High-Latitude Magnetic Field Depressions

Katariina Nykyri[1], Christina Chu[1], Xuanye Ma[1], Stephen A. Fuselier[2], and Rachel Rice[1]

[1]Physical Sciences Department and the Centre for Space and Atmospheric Research, Embry-Riddle Aeronautical University, Daytona Beach, FL, USA, [2]South West Research Institute, San Antonio, TX, USA

Key Points:
- MMS orbit can reach high-latitude dayside magnetopause and associated boundaries
- MMS observed trapped energetic electrons, protons, He^{++}, and O^{+} in magnetic field depressions likely created by low-latitude reconnection
- Counterstreaming O^{+} and He^{++} was observed in some of the depression regions

Correspondence to:
K. Nykyri,
nykyrik@erau.edu

Citation:
Nykyri, K., Chu, C., Ma, X., Fuselier, S. A., & Rice, R. (2019). First MMS observation of energetic particles trapped in high-latitude magnetic field depressions. *Journal of Geophysical Research: Space Physics*, *124*, 197–210. https://doi.org/10.1029/2018JA026131

Received 26 SEP 2018
Accepted 22 DEC 2018
Accepted article online 8 JAN 2019
Published online 19 JAN 2019

Abstract We present a case study of the Magnetospheric Multiscale (MMS) observations of the Southern Hemispheric dayside magnetospheric boundaries under southward interplanetary magnetic field direction with strong B_y component. During this event MMS encountered several magnetic field depressions characterized by enhanced plasma beta and high fluxes of high-energy electrons and ions at the dusk sector of the southern cusp region that resemble previous Cluster and Polar observations of cusp diamagnetic cavities. Based on the expected maximum magnetic shear model and magnetohydrodynamic simulations, we show that for the present event the diamagnetic cavity-like structures were formed in an unusual location. Analysis of the composition measurements of ion velocity distribution functions and magnetohydrodynamics simulations show clear evidence of the creation of a new kind of magnetic bottle structures by component reconnection occurring at lower latitudes. We propose that the high-energy particles trapped in these cavities can sometimes end up in the loss cone and leak out, providing a likely explanation for recent high-energy particle leakage events observed in the magnetosheath.

Plain Language Summary Understanding the origin, acceleration mechanisms, and ultimately predicting the space radiation environment of high-energy particles is critical for safe unmanned and manned space operations. In this article we present the first observations of the generation mechanism of a new kind of magnetic bottle at the high-latitude region of the Earth's magnetic shield with high-fluxes of high-energy particles (> 100 keV) using data from National Aeronautics and Space Administration's Magnetosphere Multiscale mission and numerical simulations. The Magnetosphere Multiscale composition measurements of He^{++}, O^{+}, H^{+}, and $e-$ as well as sensitivity to different energies allows us to calculate the size of the magnetic bottle, which for the present event was created by magnetic reconnection about 8 R_E from the spacecraft. We show the first observations of the counterstreaming O^{+} of ionospheric origin in the magnetic field depressions. We show that particles from these bottles can sometimes "leak out" to the magnetosheath providing a likely explanation for recent high-energy particle leakage event observations.

1. Introduction

Recent Magnetosphere Multiscale (MMS) observations have revealed energetic (≥ 40 keV) electrons leaking into the magnetosheath (Cohen et al., 2017). The detailed physical mechanisms explaining the origin of these particles is not understood. Although the MMS mission is designed to investigate the small-scale low-latitude physical processes (e.g., dayside reconnection and tail reconnection), its orbits can reach to the exterior cusp boundaries close to the equinoxes in 2015 and 2016 and during high dipole tilt. Close to equinoxes MMS orbit had a significant y component and therefore the z_{GSM} coordinate could be substantial (up to ≈ 5–7 R_E) meaning that the MMS orbit was actually closer to southern exterior cusp boundaries rather than the vicinity of the subsolar magnetopause at the equatorial plane. Figure 1 shows examples of MMS1 orbital plots together with Tsyganenko 96 (Tsyganenko, 1996) model in x, z plane in GSM coordinates. We show one example for each month of the MMS orbits with a circle highlighting the electron leakage event listed in Cohen et al. (2017). The interplanetary magnetic field (IMF) vector in GSM coordinates during each leakage event is marked in each panel and distance between MMS to the $y = 0$ plane is shown in bottom corner of each panel. Cluster trajectory during encounters of the "traditional" diamagnetic cavities (DMCs) at Northern (Nykyri, Otto, Adamson, Dougal, & Mumme, 2011) and Southern (Cargill et al., 2004) Hemispheres are shown for comparison. This shows that the MMS orbit can frequently encounter southern

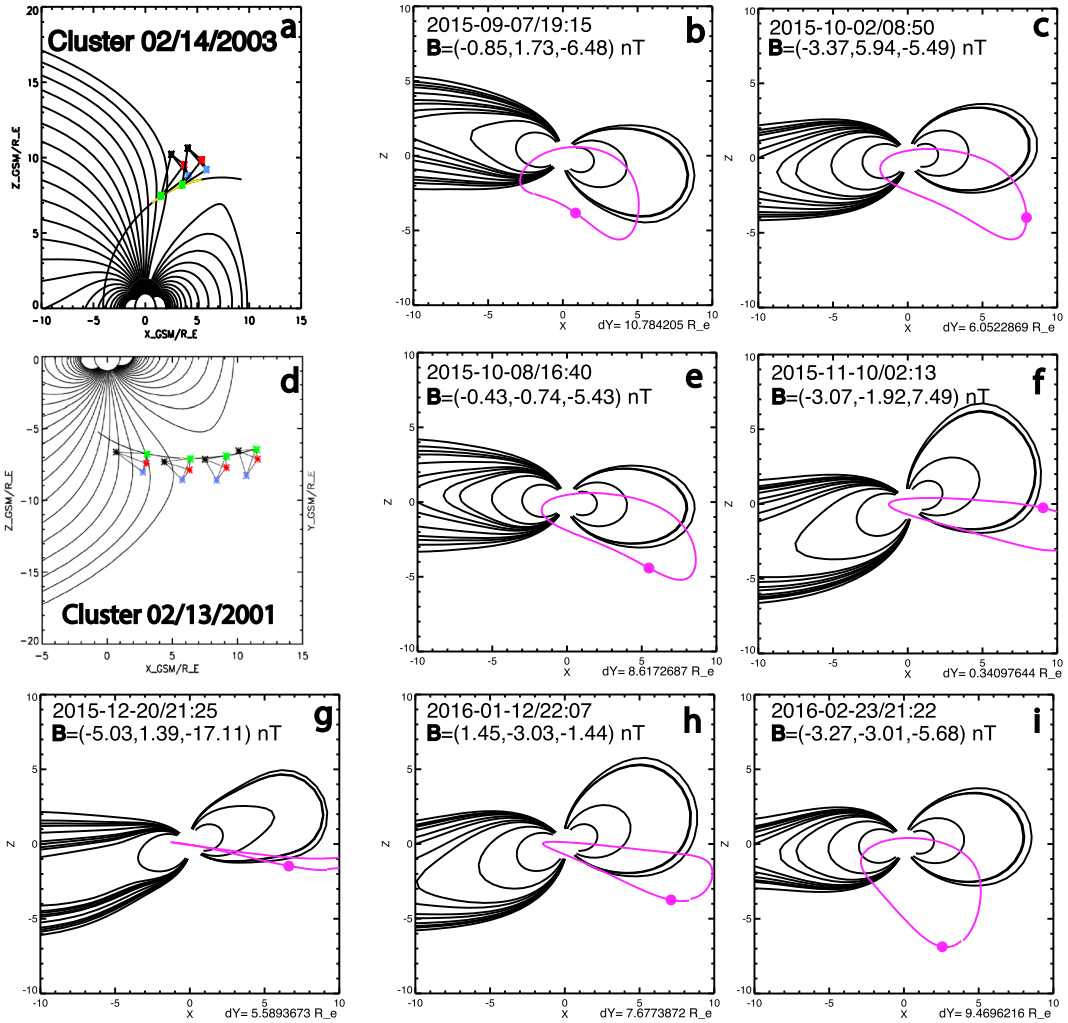

Figure 1. Example of Cluster spacecraft trajectory during northern (a) and southern (d) cusp diamagnetic cavity crossings, respectively. (b, c, e, and f–i) MMS locations close to Southern Hemisphere magnetospheric boundaries calculated from T96 model in x, z_{GSM} plane during electron leakage events observed by Cohen et al. (2017). The interplanetary magnetic field vector in GSM coordinates during each leakage event is marked in each panel and distance between MMS to $y = 0$ plane is shown in bottom corner of each panel. The present event analyzed in this paper is shown in panel (c) in same format for comparison. MMS = Magnetospheric Multiscale.

high-latitude magnetospheric boundaries, which is not always obvious if viewing data in GSE coordinate system or not considering the diurnal wobble of the geodipole. It therefore is possible that some of the MMS high-energy electron events observed in the magnetosheath originate from the "traditional" DMCs or from a new kind of magnetic bottles created by component reconnection such as discussed in the present paper.

The DMCs, characterized by extended regions of decreased magnetic field and high plasma beta surrounding the high-altitude cusp funnel, are mainly formed by magnetic reconnection between the IMF and Earth's magnetic field surrounding the magnetospheric cusps (Adamson et al., 2011, 2012; Nykyri, Otto, Adamson, Dougal, & Mumme, 2011; Nykyri, Otto, Adamson, & Tjulin, 2011; Zhang et al., 2013). Cusps are a funnel-like, basic topological features of the magnetosphere, and were first predicted by Chapman and Ferraro (1931) using the image dipole model. Observationally, cusps are typically identified as narrow regions of recently reconnected field lines which map into the ionosphere at high latitudes mostly consisting of cold, magnetosheath-like plasma and of particles propagating earthward (Wing et al., 2001). DMCs, on the other hand, are large, extended regions formed on the field lines that have reconnected sometime in the past and consist of both earthward propagating and reflected particle populations and are frequently associated with high-energy (> 30 keV) electrons, protons, and O^+ ions (Nykyri, Otto, Adamson, Dougal, & Mumme, 2011).

The O^+ outflow from the ionosphere, through the cusps, has important consequences for the global magnetospheric dynamics (Brambles et al., 2010).

While there has been considerable debate on the origin of the high-energy particles in the DMCs (Asikainen & Mursula, 2005; Chang et al., 1998; Chen & Fritz, 1998; Fuselier et al., 1991; Nykyri, Otto, Adamson, Dougal, & Mumme, 2011; Sibeck et al., 1987; Trattner et al., 2001), test particle simulations (Nykyri et al., 2012) and the presence of the high fluxes of energetic 90° pitch angle (PA) electrons and O^+ ions in strongly depressed magnetic field regions (Nykyri, Otto, Adamson, Dougal, & Mumme, 2011; Nykyri et al., 2012; Walsh et al., 2010) are consistent with local acceleration mechanisms in the cavity. Simulations in a high-resolution 3-D cusp model uncovered that trapped particles in the DMCs can be accelerated by 40 keV when their drift paths go through regions of "reconnection quasi-potential" (Nykyri et al., 2012), resulting in perpendicular acceleration and PAs of 90°. The test particle simulations showed that the efficiency of the acceleration mechanism depends on the magnitude of the draped magnetic field and how long the particles remain trapped before the IMF changes orientation. The 40-keV acceleration was achieved for the draped field of 10 nT in 6 min, but energies up to 200 keV are possible for higher draped field magnitudes (Nykyri et al., 2012) and longer trapping times. It also has been shown that the contribution of plasma waves is small on the particle acceleration in the DMCs (Nykyri, Otto, Adamson, & Tjulin, 2011).

Recently, Luo et al. (2017) performed a statistical study using 11 years of high-energy (> 274 keV) proton and oxygen data from the Cluster spacecraft. Their results indicate that the energetic ion distributions are influenced by the dawn-dusk IMF direction. Under northward IMF, their statistics for high latitudes between $4\,R_E < |Z_{GSM}| < 8\,R_E$ showed a higher flux (F) asymmetry index ($F = \frac{F_{dusk}-F_{dawn}}{F_{dusk}+F_{dawn}}$) for quadrants where the location of a DMC is predicted. During southward IMF with positive B_y, it was found that the flux intensity of H^+ is much higher at the duskside than it is at the dawnside for both the dayside magnetosphere and nightside plasma sheet in the Northern Hemisphere. In Southern Hemisphere under southward IMF and under positive IMF B_y, the asymmetry at the dayside was dawnward for both H^+ and O^+ ions in agreement with the expected DMC formation location for the most antiparallel magnetic fields.

Observational signatures of the high-altitude cusp crossings are sensitive to the orbit altitude and prevailing solar wind conditions. The Northern Hemisphere cusp crossings from Cluster revealed that reconnection tailward of the cusp during northward IMF leads to strong field-aligned flows, which are observed when spacecraft enter the reconnected cusp fields lines from the tail lobe (Nykyri et al., 2003, 2004, 2006; Vontrat-Reberac et al., 2003). The magnetic field strength during these type of cusp crossings is still large, ≈100–60 nT, and gradually decreases to ≈ 40 nT. When moving into the region of accumulated old reconnected flux, the spacecraft observe stagnant plasma. Lavraud et al. (2002) coined the "Stagnant Exterior Cusp'; this region is characterized by stagnant plasma, more isotropic ion velocity distributions, and gradual field decrease from 40 to 10 nT. Zhang et al. (2005) showed that energetic (> 28 keV) protons and energetic electrons were present during 80% and 23% of the Stagnant Exterior Cusp crossings, respectively. The encounters of the DMCs, however, have revealed very abrupt and strongly depressed magnetic field magnitudes with respect to surrounding boundaries. For example, the four Cluster spacecraft separation of 5,000 km allowed a determination of DMC structure and dynamics under northward and southward IMF (Nykyri, Otto, Adamson, Dougal, & Mumme, 2011; Nykyri, Otto, Adamson, & Tjulin, 2011). During the cavity encounter the magnetic field rapidly dropped from 80 nT (in lobe magnetosphere) to 4 nT (in cavity). When the IMF turned southward, a new cavity formed sunward of the old cavity. Cargill et al. (2004) discussed a southern cusp crossing with a rapid depression of about 60 nT in the magnetic field strength that lasted only about 5 min and coincided with higher ion temperatures and reduced densities with respect to surrounding regions.

This article presents a case study of MMS observations on 2 October 2015 of the formation of a new kind of magnetic bottle, which resembles the prior Cluster observations of the DMCs. Although the DMC was formed in unusual location, we demonstrate that the underlying generation mechanism (reconnection) is the same. The "traditional" DMCs have been observed at high latitudes during local antiparallel reconnection in the vicinity of the cusps, while here we show that DMC is formed at high latitudes by remote component reconnection at low latitudes. MMS traversed duskward from the dayside magnetosphere through the high-latitude dayside boundary layer (see Figure 2). The IMF was steady southward ($B_z \approx -6$ to -7 nT) with a strong duskward component ($B_y \approx +6$ to 8 nT), and B_x was small and varied between -1 and $+1$ nT. The solar wind velocity varied between 360 and 400 km/s, and the density varied between 3.9 and

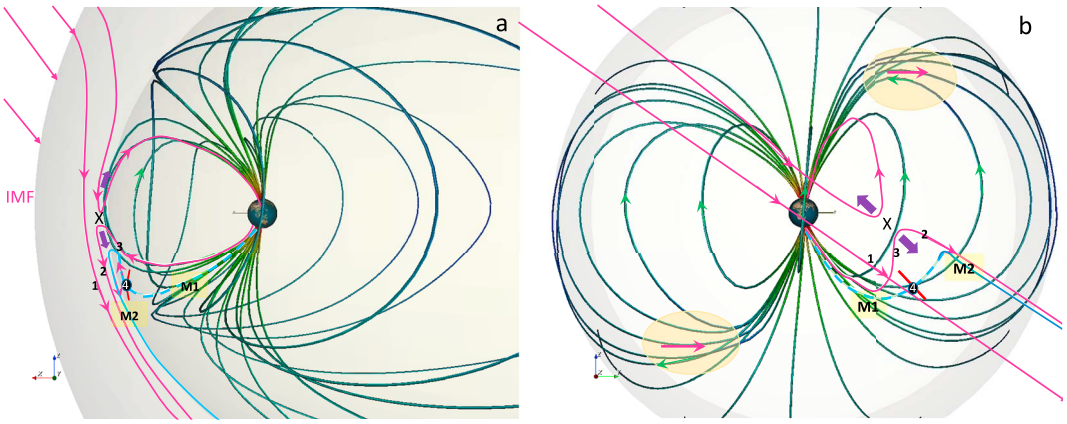

Figure 2. Three-dimensional visualization of the Earth's magnetic field topology in GSM coordinates computed using T96 model (Tsyganenko, 1996) at 9:24 UT in the *x*-*z* plane (a) and in the *y*-*z* plane (b), respectively. The MMS orbit between 8 and 11:00 and location between 09:24 are shown in red line and by a (magnified) black circle, respectively. The cartoon of field line topology resulting from component reconnection for $B_z < 0$, and $B_y > 0$ similar to Gosling et al. (1990) is visualized in top of the T96 field lines. The IMF field lines and recently (later) reconnected field lines are visualized in magenta (light blue). The dashed light blue line shows the field line mapped using T96 model from MMS location to the ionosphere and toward the equator at $t = 09{:}24$. The direction of the Earth's magnetic field, IMF, and de Hoffman-Teller frame velocity are depicted with green, magenta, and purple arrows, respectively. The numbers mark the expected locations relative to reconnection topology consistent with the velocity distribution functions shown in Figure 4. M1 and M2 mark the magnetic mirror points. The expected locations of traditional cavity formation (see Figure 6) via antiparallel reconnection are identified by large ovals in the Northern and Southern hemispheres, respectively. MMS = Magnetospheric Multiscale; IMF = interplanetary magnetic field.

5.5 cm^{-3} inducing a dynamic pressure of the order between 1.1 and 1.5 nPa during the interval. The duration of quasiperiodic encounters with the depressed field regions and high-energy particles lasted a couple of hours. In this article we show the detailed analysis of subinterval from 9:18 to 9:30 UT and describe the main properties of the other DMCs during the same event. The MMS trajectory between 8:00 and 11 UT is identified by the red trace in Figures 2a and 2b. The MMS separation is only about 20–30 km, so all spacecraft observe the same large-scale plasma and magnetic field features.

2. Methods

2.1. Instrumentation and Data Used

All magnetospheric data shown in Figures 3–5 are the level 2 data from one of the National Aeronautics and Space Administration's MMS satellites (MMS1; Burch et al., 2016). We use Hot Plasma Composition Analyzer (HPCA) for the H^+, He^{++}, and O^+ ion phase space-energy spectrograms and velocity distribution functions (Young et al., 2016); Fast Plasma Investigation (Pollock et al., 2016) for the ion energy spectra and moments; and Flux Gate Magnetometers (Russell et al., 2016; Torbert et al., 2016) for the DC magnetic field. Energetic electron distribution and PA data come from the Fly's Eye Energetic Particle Spectrometer (Blake et al., 2016) instrument. Energetic (49–209 keV) proton PA data are available from the Energetic Ion Spectrometer (Mauk et al., 2016). The versions of the data files used are v4.18.0.cdf, v3.1.0.cdf, v3.2.0.cdf, v6.0.1.cdf, v3.0.0.cdf, and v2.1.0.cdf for Flux Gate Magnetometers, Fast Plasma Investigation, HPCA, Fly's Eye Energetic Particle Spectrometer, and Energetic Ion Spectrometer, respectively. Solar wind conditions are taken from the OMNI (http://omniweb.gsfc.nasa.gov/) database (King & Papitashvili, 2005).

2.2. Loss Cone PA Calculation

The loss cone PA, α, shown in Figures 4l and 4m with black curves,

$$\alpha = \arctan\left(\frac{1}{\sqrt{B_M/B - 1}}\right), \tag{1}$$

uses a constant magnetic field value at the mirror point, $B_M = 45$ nT, and B is the magnetic field magnitude observed between 9:18 and 9:30 UT (including the cavity interval). Figures 4l and 4m shows that a 45-nT field at the mirror point is able to trap most of the particles in the cavity region where the field is about 25 nT. The magnetic bottle structure between mirror points M1 and M2 is illustrated in Figure 2 and later

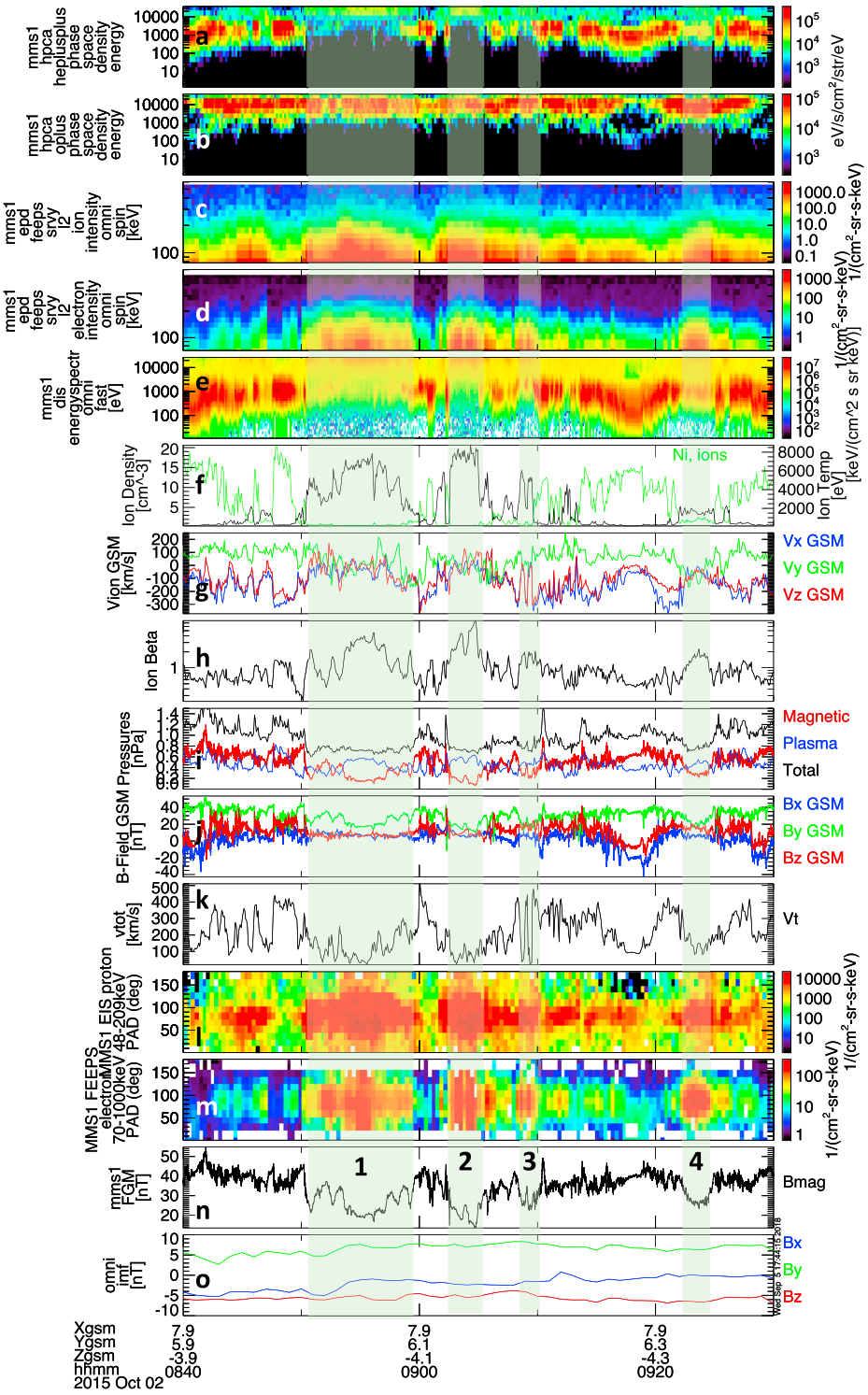

Figure 3. MMS1 observations between 8:40 and 9:30 of (a) He^{++}; (b) O^{+}; (c) omnidirectional energetic ion intensity; (d) omnidirectional energetic electron intensity; (e) lower-energy protons; (f) ion density (green) and temperature; (g) ion velocity; (h) ion plasma beta; (i) magnetic, plasma, and total pressure; (j) magnetic field; (k) total velocity; 48- to 209-keV energetic proton (l) and 70–1,000 keV energetic electron (m) pitch angle distributions; (n) total magnetic field strength; (o) and the IMF from OMNI. The four main cavities are highlighted with green boxes. MMS = Magnetospheric Multiscale; HPCA = Hot Plasma Composition Analyzer; FEEPS = Fly's Eye Energetic Particle Spectrometer; EIS = Energetic Ion Spectrometer; IMF = interplanetary magnetic field.

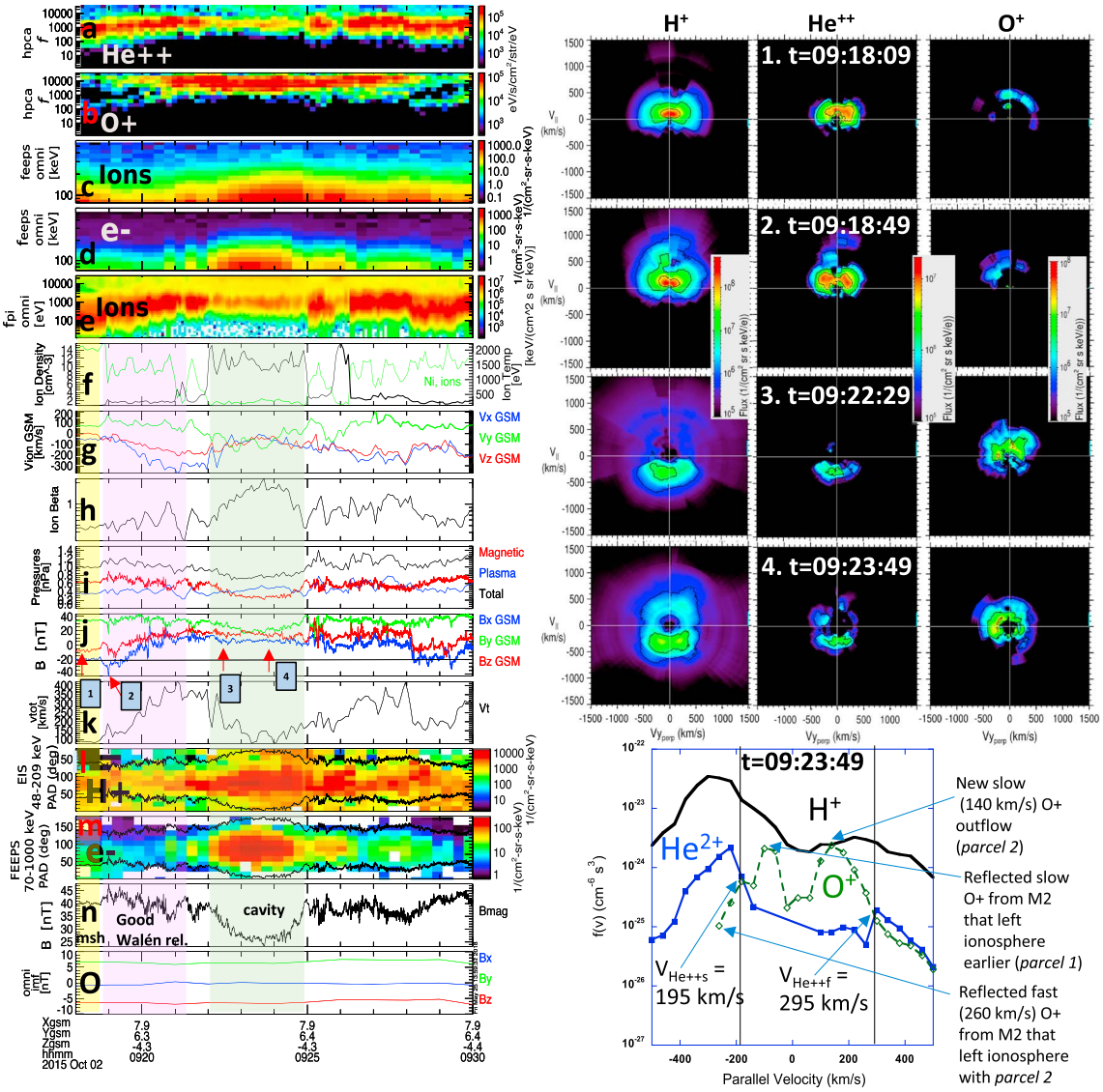

Figure 4. MMS1 observations between 9:18 and 9:30 of the plasma and field properties (panels a–n) and OMNI magnetic field (panel o). The loss cone PA is highlighted by black lines for energetic protons (l) and electrons (m). On the right are the H^+, He^{++}, and O^+ velocity distribution functions at four different times: at the msh-side (1), at the reconnected field line on the msh-side (2) and magnetospheric side (3), and at the "older" reconnected field line (cavity; 4). The observation times of these distributions relative to magnetic field are marked with red arrows (k). The parallel cut of the phase space density for distribution 4 is shown for H^+, He^{++}, and O^+. MMS = Magnetospheric Multiscale; HPCA = Hot Plasma Composition Analyzer; FEEPS = Fly's Eye Energetic Particle Spectrometer; EIS = Energetic Ion Spectrometer; IMF = interplanetary magnetic field.

in Figure 6f. The mirror point, M2, is formed at the magnetospheric side of the cumulated reconnected field lines which increases the magnetic field strength in this region.

2.3. Global MHD Modeling

In order to put the MMS observations in the context of the magnetospheric boundaries and to estimate the distance to the mirror point M1, where field strength becomes 45 nT, we have simulated the event from 08:00 to 11:00 UT using Space Weather Modeling Framework (SWMF/BATSRUS; De Zeeuw et al., 2004; Powell et al., 1999; Ridley & Liemohn, 2002; Tóth et al., 2005, 2012; Wolf et al., 1982) using 34.7-M cells and 1/16 R_E numerical resolution at the inner boundary. However, the detailed physical process of the particle dynamics in the DMCs requires a more sophisticated comparison between global simulations with test particles and in situ observations, which will be addressed in our future study. The run results and model settings can be found at the National Aeronautics and Space Administration community coordinated modeling center (https://ccmc.gsfc.nasa.gov/results) with the following run ID: *Katariina_Nykyri*_020918_2.

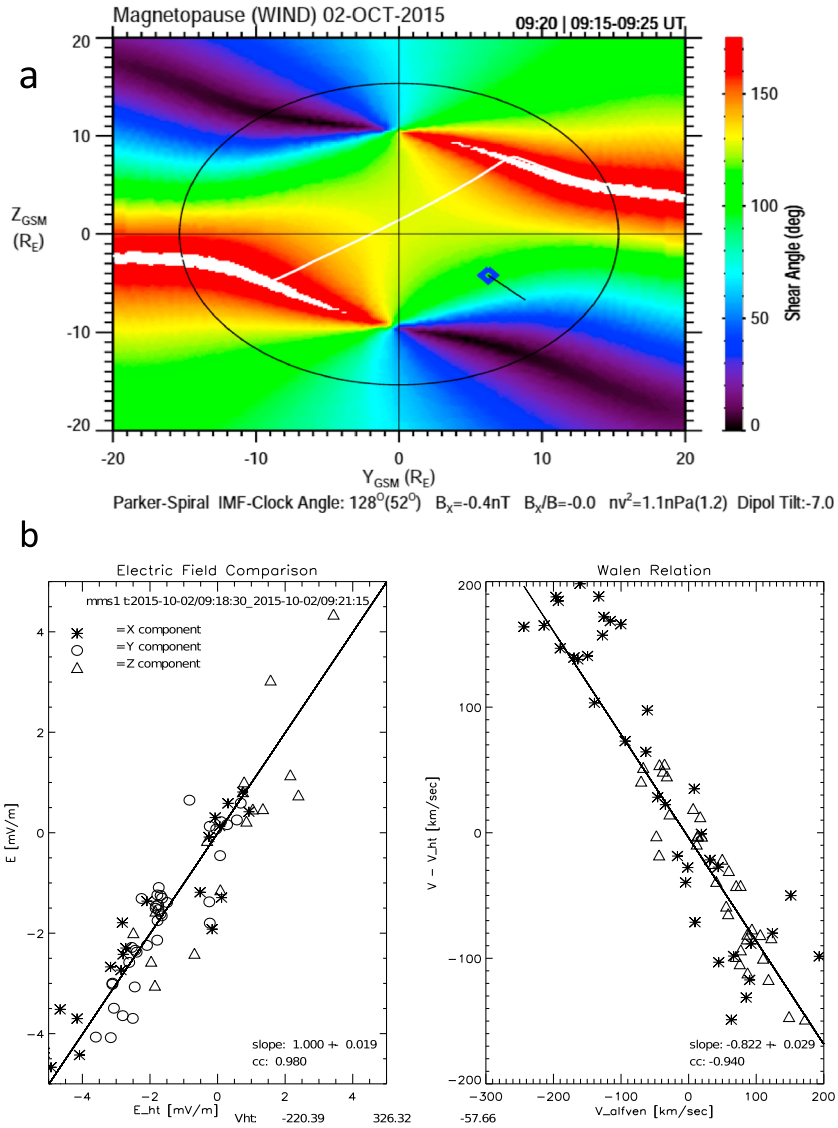

Figure 5. Maximum magnetic shear model illustrating the angle between the draped interplanetary magnetic field (IMF; from lagged Wind data) and Earth's magnetic field at the magnetopause (a). Magnetospheric Multiscale location is marked with blue square and IMF direction with black line. The $-\mathbf{v} \times \mathbf{B}$ electric field comparison with the de Hoffman-Teller frame electric field and the Walén relation calculated from the Fast Plasma Investigation instrument using the pressure anisotropy correction (b).

3. Results

3.1. MMS Observations

Figures 3 and 4 present MMS1 observations of plasma and magnetic field properties on 2 October 2015 between 08:40–9:30 and 09:18–09:30 UT, respectively, at the high-latitude dayside magnetospheric boundary. During 8:40–9:30 MMS moved duskward (from $y = 5.9\ R_E$ to $y = 6.3\ R_E$) and southward (from $z = -3.9\ R_E$ to $z = -4.3\ R_E$) and had multiple encounters of high-energy particles in the depressed field regions.

We next focus on detailed analysis of the subinterval between 09:18 and 09:30 (4th cavity in Figure 3) when MMS was located at the ($R \approx$[7.9, 6.4, -4.3]; see Figure 4). Between 9:18 and 9:18:40 UT MMS was at the open magnetosheath (msh) field lines close to the magnetopause that map to the quasi-parallel shock at the northern hemisphere (msh, yellow highlighted column). This msh-interval is characterized by high fluxes of He^{++}, which is a typical signature of solar wind source (a), lower fluxes of 48- to 209-keV ions (c), high fluxes of low-energy ions (e) with lower temperatures and higher ion densities (f) than the subsequent cavity interval. Between ≈ 9:19 and 9:21:15 MMS encounters gradually increasing strong tailward plasma flows (g) and a

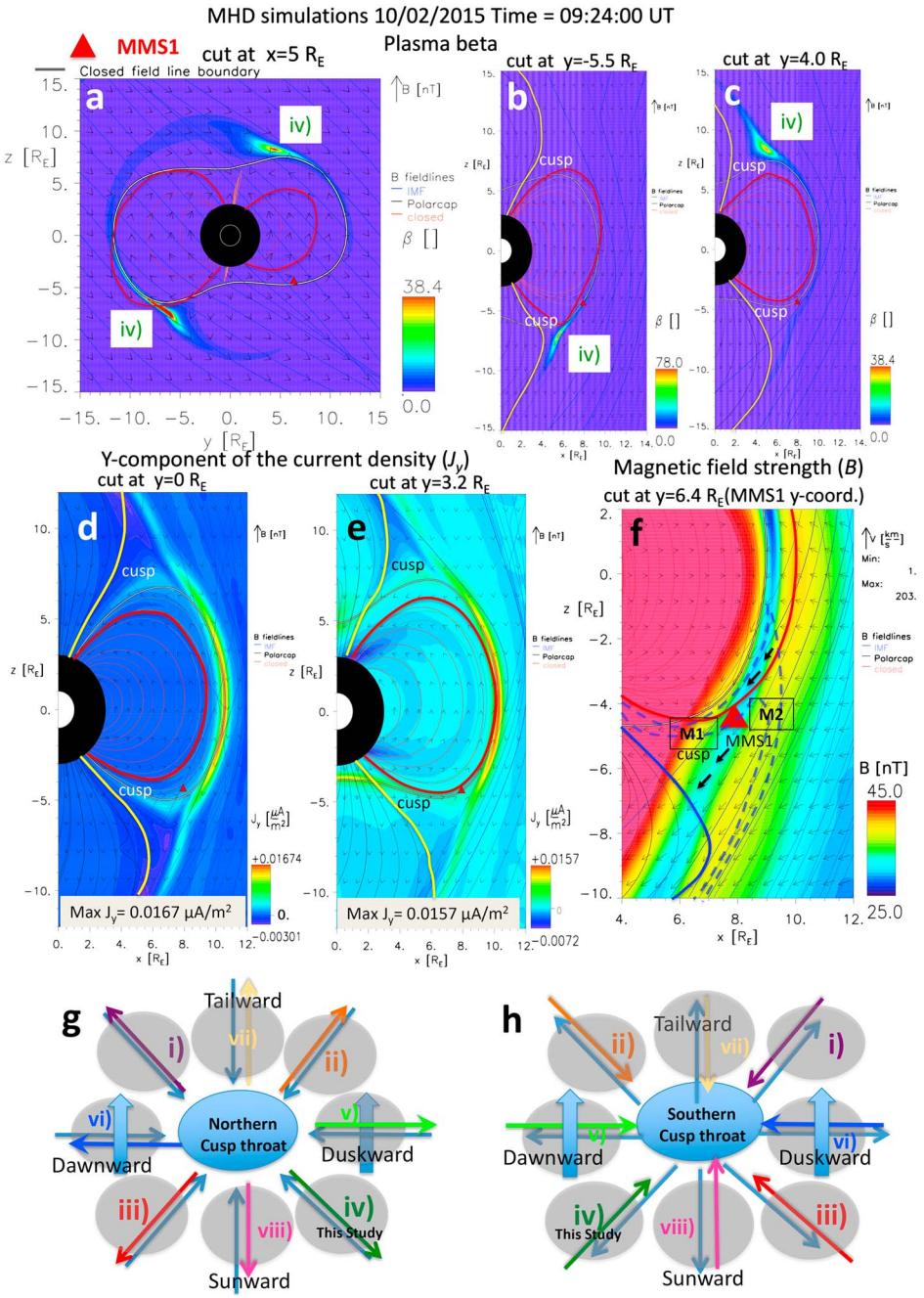

Figure 6. MHD model results at 9:24 UT of plasma beta and magnetic field vectors in y, z plane at $x = 5\ R_E$ (a), in x, z plane at $y = -5.5\ R_E$ (b), and at $y = 4\ R_E$ (c). The y component of the current density, J_y, (color) and magnetic field vectors in x, z plane at $y = 0$ (d) and at $y = 3.2\ R_E$ (e). The magnetic field strength and velocity vectors in x, z plane at the MMS1 y coordinate, $y = 6.4\ R_E$ (f). The last closed and the first polar cap field line tailward of the cusp are overplotted with thick, red and yellow lines, respectively (instead of yellow, blue color is used in panel f to distinguish the line from background). Diagram of the expected locations (gray ovals) of the diamagnetic cavities for different IMF orientations at the vicinity of the northern (g) and southern (h) cusps. Gray arrows present the direction of Earth's magnetic field and colored arrows present the direction of the draped IMF for the following main IMF B_y and B_z conditions: (i) $B_y < 0, B_z > 0$, (ii) $B_y > 0, B_z > 0$, (iii) $B_y < 0, B_z < 0$, (iv) $B_y > 0, B_z < 0$, (v) $B_y \gg |B_z|$, (vi) $B_y \ll -|B_z|$, (vii) $B_z \gg |B_y|$, and (viii) $B_z \ll -|B_y|$. The blue thick arrows present regions where B field is perpendicular to the magnetosheath flow. MHD = magnetohydrodynamics; MMS = Magnetospheric Multiscale; IMF = interplanetary magnetic field.

magnetic field rotation (j). The plasma density decreases from the magnetosheath values to about 6–11 cm^{-3} and temperature increases slightly (f). The magnetic field strength (n) shows about 30-s oscillations with about 10-nT amplitude, creating a wavy signature in ion-beta (h). The combination of the magnetic field and plasma flow changes, as well as the magnetic field topology in Figures 2a and 2b, is consistent with the MMS trajectory from the magnetosheath (ion distribution 1) through the rotational discontinuity where B_x and B_z first become more negative (ion distribution 2) when MMS enters the magnetosheath side of the reconnected field line, and then gradually turn positive when MMS moves to the magnetospheric side of the reconnected field line (ion distribution 3). The B_y is positive (j) both on draped IMF field lines and on Earth's magnetic field lines in this location as can be expected based on T96 model and MMS position (see Figure 2b) and from the global magnetohydrodynamics (MHD) model (see Figure 6a).

By 9:24 the magnetic field strength (n) has decreased by 22 nT from the values observed during the encounter of the msh-side of the reconnected field line at 9:18:53. Meanwhile, the thermal pressure increases in the magnetic cavity. However the total pressure is still lower than outside of the cavity (i). Reduced magnetic pressure, balanced by the increased thermal pressure is a typical signature of the diamagnetic cusp cavities created by reconnection in MHD (Adamson et al., 2012). Here the plasma pressure calculation does not include the high-energy particles, which is why the plasma pressure does not balance the magnetic pressure. Similar to southern cusp event observed by Cargill et al. (2004), the density has reduced, and temperature has increased from the values in the surrounding regions. Inside the main cavity, the lower-energy part of the He^{++} population has increased in energy from the typical magnetosheath values of $\approx$ 100 eV to 2 keV to 900 eV to 2 keV, and there also appears a higher energy population between 10 and 30 keV with $\sim$ 10 times lower phase space densities than the 800 eV to 30 keV population in the cavity (a). The depressed field region correlates also with enhanced fluxes of high-energy 1- to 30-keV O^+ ions (b), 80- to 209-keV protons (c), and 70- to 300-keV electrons (d). The PA plots (panels l and m) are shown in the spacecraft frame. In these PA plots, the black lines represent the boundary of the loss cone for the particles inside the cavity: assuming adiabatic particle motion the particles that have PAs between the black lines are trapped and cannot originate from the higher magnetic field region directly without some reprocessing. In particular, the 70- to 1,000-keV electrons appear to be well trapped in the depressed field regions. In the magnetosheath (yellow box) there exists parallel high-energy proton fluxes. These parallel protons close to the magnetopause boundary could originate from the quasi-parallel bow shock (Trattner et al., 2011) at the Northern Hemisphere or result from leakage out of the cavity through weaker mirror point M2 (see Figures 2 and 6). For a Gaussian distribution, if bulk velocity is perpendicular to the magnetic field, one would expect a strong 90° PA distribution. In contrast, the observation only shows a weak flux at the 90° PA during the good Walén relation region (characterized by strong, mostly perpendicular flow), indicating that in bulk-velocity frame most particles move along the field line. In the magnetosheath the low bulk velocity is mostly along the magnetic field direction. However, the distribution 1 is still asymmetric; therefore, a field-aligned anisotropy is evident in the HPCA distribution. This anisotropy likely extends into the energetic particle data, which is consistent with the ion spectra in panel l.

The right-hand side of Figure 4 shows HPCA ion velocity distribution functions for H^+, He^{++}, and O^+ at four different times (marked with the numbered boxes in Figures 2a and 2b and left side of the Figure 4). These distributions are shown in the frame where the velocity of the H^+ distribution perpendicular to the magnetic field is zero. The H^+ and He^{++} velocity distribution functions in the magnetosheath between t = 9:18:04–9:18:14 (row 1) show a typical parallel streaming low-energy core distribution. Unlike He^{++}, the H^+ distribution shows also a higher-energy population extending to about 1,200 km/s. Between t = 9:18:44–9:18:54 (row 2) MMS has moved onto the newly reconnected field line (on the magnetosheath side) and the high-energy H^+ population becomes prominent covering a wide range of PAs in the parallel direction. Meanwhile, the low-velocity core of the H^+ and He^{++} distributions are shifted along the magnetic field direction. The He^{++} distribution also shows a high-energy population in the parallel direction, indicating that at least part of this population is reflected off the open magnetopause. The O^+ distribution is also streaming parallel to the magnetic field and indicates that there is escape of magnetospheric ions along open field lines into the magnetosheath.

By t = 9:22:24–09:22:34 (row 3) MMS has moved to the magnetospheric side of the recently reconnected field line and observes an antiparallel lower-energy population of solar wind origin, while the high-energy H^+ population becomes more isotropic. He^{++} shows the low-energy, antiparallel propagating population as well. The direction of propagation is consistent with a reconnection site northward of the spacecraft

Table 1
Properties of Ion Velocity Distribution Functions During Cavity Observations Shown in Figure 3

Cavity	O^+	H^+	He^{++}
1	CS low energy and high energy	CS low energy and high energy	CS low energy and high energy
2	CS low energy and high energy	high energy	high energy
3	CS low energy and high energy	CS low energy and high energy	CS low (at exit) and high energy
4	CS low energy and high energy	CS low energy and high energy	CS low energy and high energy

Note. Counterstreaming (CS) low-energy or high-energy populations are indicated. The low-energy He^{++} and H^+ originate from the magnetosheath, while the low-energy O^+ originates from the ionosphere. The high-energy populations are either ring current or locally accelerated.

location. O^+ distribution is propagating mostly in parallel direction, due to outflow from the ionosphere. At t = 9:23:44–09:23:54 (row 4) MMS encounters a field line that has been opened by reconnection for a longer period of time and observes both the incoming lower and higher energy solar wind H^+ population (antiparallel to magnetic field), as well as the enhanced and reflected (parallel to magnetic field) low-energy population from the Southern Hemisphere ionosphere. The symmetric high-energy H^+ population at 9:22:29 and 9:23:49 are very similar as the high-energy particles travel faster to the mirror points M1 and M2 (shown in Figure 2). Both the He^{++} and O^+ show the incoming and reflected low-energy populations. The parallel (with respect to magnetic field) cut of the phase space density during the cavity interval at 09:23:49 clearly demonstrate the incoming and reflected low-energy populations for H^+ and He^{++}, as well as the fresh ionospheric outflow (parcel 2) of O^+ parallel to magnetic field which gets reflected at the M2 mirror point in the spine region of the cumulated reconnected flux. This reflected low-energy O^+ population (parcel 1) is likely visible because it left the ionosphere slightly earlier (this is the parallel population in the 3rd O^+ distribution seen 80 s earlier) than parcel 2 and due to large gyroradius of O^+.

The color code in Figure 5a shows the angle between draped IMF and Earth's magnetic field at the magnetopause illustrating that regions with the most antiparallel fields exists at the dusk sector of the northern cusp and at the dawn sector of the southern cusp (expected location of traditional DMCs). The shear angles were calculated using the maximum shear model developed by Trattner et al. (2007) where the geomagnetic field direction is given by the T96 model and the draped IMF conditions at the magnetopause are calculated using the model by Cooling et al. (2000). It can be seen that magnetic shear is significant (100–120°) in the extended region above MMS which can result in component reconnection. Figure 5b shows that during 9:18:30–9:21:15 UT there exists an excellent de Hoffman-Teller (HT) frame (slope = 1 and correlation coefficient = 0.94), and a good Walén relation (slope = −0.822 and cc. = −0.94). The HT velocity is [−220,326,−58] km/s and is consistent with the direction of purple arrows in Figures 2a and 2b. These HT frame velocities and good Walén relations are further evidence for the component reconnection for the prevailing ≈ 130° IMF clock angle (Fuselier et al., 2011; Gosling et al., 1990) occurring northward and dawnward of the MMS location. This field line topology highlighted in Figure 2 agrees with our interpretation of the H^+, He^{++}, and O^+ velocity distribution functions when MMS crosses from the magnetosheath onto reconnect field lines. The Walén relations during the transitions into the cavity between 9:21:15 and 9:23:15, and out of the cavity between 09:23:15 and 09:25:30 were not satisfied (−0.25 and −0.01, respectively) apparently because of the reflected populations. Also, the latter interval with the flow enhancement between 09:26:00 and 09:30:00 did not satisfy the Walén relation. The Wálen relation was not satisfied for the plasma flows before the observation of the other three main cavity intervals shown in Figure 3.

Table 1 summarizes the properties of the ion velocity distributions observed in the four cavities. Cavities 1 and 3 have similarities with cavity 4. They all have intervals when there is counterstreaming O^+, He^{++}, and H^+. For He^{++}, this counterstreaming population is at approximately 1–5 keV/e in Figure 3. The presence of counterstreaming O^+ is indicative of a source from the southern ionosphere and reflection at M2. The presence of counterstreaming He^{++} is indicative of a magnetosheath source and reflection in the M1. H^+ is a mixture of both the magnetosheath and magnetospheric sources. The difference between cavities 1 and 3 and cavity 4 is that the counterstreaming populations are observed throughout cavity 4 and only intermittently, in particular at the entrance and exit, of cavities 1 and 3. The distributions in the center of cavities 1 and 2 are similar to the distributions in cavity 3. Cavity 3 is different from cavities 1 and 4 in that there is no counterstreaming He^{++} except possibly at the exit of the cavity at 0910 UT. Otherwise, the centers of cavities

1 and 2 and most of cavity 3 appear to be consistent with ring current-like energies above 10 keV for He^{++}. The transition from a mixture of magnetospheric and magnetosheath ions into a region where there are only magnetospheric ions is consistent with a transition from the cavity to the outer magnetosphere.

3.2. MHD Simulations

Figure 6 shows the plasma and field properties of the dayside magnetosphere at 09:24 UT from high-resolution MHD global simulation results, with the MMS1 location projected in each plane as well as the cartoon of the expected DMC locations based on the maximum shear of the draped IMF field around the geomagnetic field in the vicinity of the cusps. The DMCs are directly generated by reconnection in maximum magnetic shear regions in a similar manner described by Nykyri, Otto, Adamson, Dougal, and Mumme (2011) and Adamson et al. (2011, 2012). These cavities are indicated by a strongly enhanced plasma beta (color scale is saturated at beta = 38 in order to better see the northern hemisphere DMC in the same plane) tailward of the MMS at $x = 5\ R_E$ (panel a) in the expected regions in Southern (region iv in panels b and g) and Northern Hemispheres (region iv in panels c and h). For the dipole tilt and solar wind conditions, the southern DMC at the dawn sector is more pronounced (maximum beta is 78 for cut at y = -5.5 R_E) than the DMC in the Northern Hemisphere dusk sector (maximum beta is 38 for $y = 4\ R_E$). The y component of the current density (J_y) in the x, z plane with a cut at the $y = 0$ (d) and $y = 3.2$ (e) shows that J_y is enhanced in the extended region around dayside magnetopause. This enhancement can lead to reconnection. The magnetic field strength in the x, z plane (panel f) with a cut at the MMS location ($y = 6.4\ R_E$) shows that there exists a flow channel (black vectors whose direction is consistent with the observed HT frame velocity vectors in Figure 5b) originating from an equatorial reconnection region resulting in an extended region of depressed magnetic field which is surrounded by higher magnetic field. The dashed blue line is sketched over the simulation and illustrates the topology of the magnetic bottle (projected in the x, z plane similar to Figure 2a) with the mirror points M1 and M2 at the ionospheric side and in the spine region of the reconnected flux tube, respectively. Note that the color scale is saturated here at 45 nT as this value at mirror point was sufficient in trapping most of the high-energy particles (as illustrated by narrow loss cone in Figures 4l and 4m). On the magnetospheric side of the reconnected field line, the particles move anti-parallel to the field toward the ionosphere and get reflected at M1 (about 2–2.5 R_E from MMS) when the mirror force becomes sufficient. Then they travel back over the kink region of the reconnected field line parallel to magnetic field into the spine region characterized by strongly compressed magnetic field. In the simulation, the field strength in this region is around 37 nT, while in MMS observations (see Figure 4o) the field strength on the magnetosheath side of the reconnected field line is around 48 nT at 9:19 and around 42 nT at 9:25. This is likely the leaky side of the magnetic bottle as can be seen by the energetic protons in the loss cone at 9:23:30–9:25:30 in Figure 4l when the field strength is 37–42 nT. We also produced the cuts along the simulated MMS orbit of the magnetic field, plasma flow velocity, density, and temperature (not shown). The range of density (n), temperature (T), velocity (v_x, v_y, v_z), and magnetic field (b_x, b_y, b_z and b_t) variation between 9:18 and 9:30 UT are as follows: n = [4.3,9.4] cm^{-3}, T =[3.5,6.5] MK, v_x =[−130,−100] km/s, v_y =[80, 105] km/s, v_z =[−150, −110] km/s, b_x =[−9,−4] nT, b_y =[27, 38] nT, b_z =[4, 14] nT, and b_T =[29, 36] nT. This indicates that the virtual spacecraft, unlike MMS, does not observe such fast flows or magnetic field rotations. The reconnection in the present MHD simulation operates due to numerical resistivity, which results in smoothed magnetic field and flow profiles in comparison to the real system.

4. Estimation of the MMS Distance to the Reconnection Site and M2

Because H^+ can have multiple sources, we use the parallel cuts of the O^+ (of ionospheric origin) phase space density and He^{++} (of solar wind origin) to evaluate distance to the reconnection site (L_R) using method similar to Fuselier et al. (2000) and Trattner et al. (2007). Using the estimated distance from MMS to the M1, L_{M1} = 2–2.5 R_E shown in MHD simulation (Figure 6f), the distance to L_R can be roughly estimated as

$$V_{He_f^{++}} t_1 = L_R + L_{M1} + L_{M1}$$
$$V_{He_s^{++}} t_1 = L_R$$

where t_1 is the travel time of slow (s) and fast (f) He^{++} ions from reconnection site to satellite location and from reconnection site to M1 and back to satellite location, respectively. The ion outflow using O^+ is

subtracted from the He^{++} giving $V_{He_f^{++}} = 295$ km/s and $V_{He_s^{++}} = 195$ km/s which gives:

$$L_R = \frac{2V_{He_s^{++}}L_{M1}}{V_{He_f^{++}} - V_{He_s^{++}}} = 7.8 - 9.8 \quad R_E$$

This estimated distance of 8–10 R_E from MMS to the reconnection site is in good agreement with the distance between MMS and the region of maximum magnetic shear shown in Figure 5a northward and dawnward of the MMS.

To estimate the distance to M2 we use the fast ($V_{O_f^+} = 260$ km/s), reflected O^+ from M2 and the slow ($V_{O_s^+} = 140$ km/s) O^+ originating from ionosphere through M1:

$$V_{O_f^+}t_1 = L_{M1} + L_{M2} + L_{M2} = L_{M1} + 2L_{M2}$$
$$V_{O_s^+}t_1 = L_{M1}$$
$$L_{M2} = \frac{V_{O_f^+} - V_{O_s^+}}{2V_{O_s^+}}L_{M1} = 0.9 - 1.1R_E$$

This indicates that the length of the magnetic bottle ($L_{M1} + L_{M2}$) is about 3–4 R_E. The gradient of B of about 20 nT from the center of the bottle toward the both mirror points is efficient in trapping most of the particle flux as can be estimated from mirror force calculation at M1 for 1-keV He^{++} (see Figure 4a) in the cavity and comparing it with the force required to make He^{++} parallel velocity ($v_\parallel = 295$ km/s) at distance L_{M1} zero:

$$\mu\Delta_\parallel B = \frac{1\,\text{keV}}{25\,\text{nT}}\frac{(45 - 25\,\text{nT})}{(2\,\text{to}\,2.5R_E)} = 8 - 10\text{e}^{-24} \quad \text{N}$$

$m_{He^{++}}\frac{dv_\parallel}{dt} = \frac{2*1.67\text{e}^{-27} \quad \text{kg}*295 \quad \text{km/s}}{(86 \quad \text{to} \quad 108 \quad \text{s})} = 9\text{–}11\text{e}^{-27}$ N, where the time difference of 86–108 s is estimated from $\Delta t = \frac{L_{M1}}{\frac{1}{2}v_\parallel}$. This estimation shows that the mirror force is over two orders of magnitude greater than the force required to make the He^{++} parallel velocity zero at M1.

5. Conclusions and Discussion

We have shown that MMS orbit can reach high-latitude dayside magnetopause and associated boundaries. The main conclusions can be summarized as follows:

1. Ion velocity distribution functions and good Walén relation and HT frame velocity suggest reconnection occurring dawnward and above MMS, about 8–10 R_E from MMS, which is consistent with MHD simulation.
2. MMS observed high fluxes of trapped high-energy electrons and ions in the magnetic bottle-like structure. Formation of the magnetic bottle via reconnection was also observed in the MHD simulation.
3. He^{++} (of solar wind origin) and O^+ (of ionospheric origin) phase space densities suggest that the magnetic bottle between mirror points M1 and M2 was formed by cumulation of magnetic flux in the magnetosheath originating from reconnection about 8–10 R_E from the MMS location.

We propose that the local antiparallel reconnection in the vicinity of the cusps, such as observed by Nykyri, Otto, Adamson, Dougal, and & Mumme (2011), results into the formation of stronger magnetic field depressions (~50–80 nT) than the component reconnection that was operating and created the elongated cavity for the present event. Our future work is to better understand the relative contributions of local physical mechanisms (e.g., acceleration via gradients in reconnection quasi-potential, Nykyri et al., 2012; wave acceleration, Nykyri et al., 2004; and Kelvin-Helmholtz Instability-driven processes Moore et al., 2016; Sorathia et al., 2017) and remote sources (ring current, Pulkkinen et al., 2001, and foreshock energetic particles, Trattner et al., 2011) contributing to these enhanced fluxes of energetic electrons and ions in these cavities. It is noteworthy that for the present event the IMF orientation and plasma conditions remained quite steady for hours, allowing reconnection site to remain relatively stable, and lead to formation of cavities along MMS trajectory. This stable IMF can lead to longer trapping times and therefore more efficient acceleration by the electric field in the cavity (Nykyri et al., 2012). However, Figure 4l shows that during present event some of the high-energy protons at ≈ 9:25 get into a loss cone leaking into the ionosphere or into the magnetosheath

from the cavity, while the IMF remains steady. It is possible that when the IMF changes orientation, the electrons, which are more easily to be adiabatic and trapped, could leak out, contributing to the > 40-keV electron leakage events observed by Cohen et al. (2017).

Acknowledgments
The work of K. N. and R. R. is supported by NASA grant NNX17AI50G and by NSF grant 1707521. Work by C. C. and X. M. is supported by NASA grant NNX16AF89G. Research at SWRI is supported by the NASA MMS contract. All MMS data were downloaded through the MMS Science Data Center accessible at https://lasp.colorado.edu/mms/sdc/public/, and we recognize the efforts from MMS instrument teams and all who contribute to this service. We acknowledge use of NASA/GSFC's Space Physics Data Facility's OMNIWeb (http://omniweb.gsfc.nasa.gov) service and Orbit Visualization Tool (https://ovt.irfu.se). This work was carried out using the SWMF/BATSRUS tools developed at the U. of Michigan Center for Space Environment Modeling (CSEM) and made available through the NASA CCMC at GSFC through their public Runs on Request system (http://ccmc.gsfc.nasa.gov).

References

Adamson, E., Otto, A., & Nykyri, K. (2011). 3-D mesoscale MHD simulations of a cusp-like magnetic configuration: Method and first results. *Annales Geophysicae*, *29*, 759–770. https://doi.org/10.5194/angeo-29-759-2011

Adamson, E., Otto, A., & Nykyri, K. (2012). 3-D mesoscale MHD simulations of magnetospheric cusp-like configurations: Cusp diamagnetic cavities and boundary structure. *Annales Geophysicae*, *30*, 325–341. https://doi.org/10.5194/angeo-30-325-2012

Asikainen, T., & Mursula, K. (2005). Energetic particle fluxes in the exterior cusp and the high-latitude dayside magnetosphere: Statistical results from the cluster/rapid instrument. *Annales Geophysicae*, *23*(6), 2217–2230. https://doi.org/10.5194/angeo-23-2217-2005

Blake, J. B., Mauk, B. H., Baker, D. N., Carranza, P., Clemmons, J. H., Craft, J., et al. (2016). The Fly's Eye Energetic Particle Spectrometer (FEEPS) sensors for the Magnetospheric Multiscale (MMS) mission. *Space Science Reviews*, *199*, 309–329. https://doi.org/10.1007/s11214-015-0163-x

Brambles, O. J., Lotko, W., Damiano, P. A., Zhang, B., Wiltberger, M., & Lyon, J. (2010). Effects of causally driven cusp O+ outflow on the storm time magnetosphere-ionosphere system using a multifluid global simulation. *Journal of Geophysical Research*, *115*, A00J04. https://doi.org/10.1029/2010JA015469

Burch, J. L., Moore, T. E., Torbert, R. B., & Giles, B. L. (2016). Magnetospheric Multiscale overview and science objectives. *Space Science Reviews*, *199*, 5–21. https://doi.org/10.1007/s11214-015-0164-9

Cargill, P. J., Dunlop, M. W., Lavraud, B., Elphic, R. C., Holland, D. L., Nykyri, K., et al. (2004). Cluster encounters with the high altitude cusp: Boundary structure and magnetic field depletions. *Annales Geophysicae*, *22*(5), 1739–1754. https://doi.org/10.5194/angeo-22-1739-2004

Chang, S., Scudder, J. D., Fuselier, S. A., Fennell, J. F., Trattner, K. J., Pickett, J. S., et al. (1998). Cusp energetic ions: A bow shock source. *Journal of Geophysical Research*, *25*, 3729–3732. https://doi.org/10.1029/98GL52808

Chapman, S., & Ferraro, V. C. A. (1931). A new theory of magnetic storms. *Terrestrial Magnetism and Atmospheric Electricity*, *36*, 77–97. https://doi.org/10.1029/TE036i002p00077

Chen, J. S., & Fritz, T. A. (1998). Correlation of cusp MeV helium with turbulent ULF power spectra and its implications. *Geophysical Research Letters*, *25*, 4113–4116. https://doi.org/10.1029/1998GL900122

Cohen, I. J., Mauk, B. H., Anderson, B. J., Westlake, J. H., Sibeck, D. G., Turner, D. L., et al. (2017). Statistical analysis of MMS observations of energetic electron escape observed at/beyond the dayside magnetopause. *Journal of Geophysical Research: Space Physics*, *122*, 9440–9463. https://doi.org/10.1002/2017JA024401

Cooling, B. M. A., Owen, C. J., & Schwartz, S. J. (2000). Role of the magnetosheath flow in determining the motion of open flux tubes. *Journal of Geophysical Research*, *106*(A9), 18,763–18,775. https://doi.org/10.1029/2000JA000455

De Zeeuw, D. L., Sazykin, S., Wolf, R. A., Gombosi, T. I., Ridley, A. J., & Tóth, G. (2004). Coupling of a global MHD code and an inner magnetospheric model: Initial results. *Journal of Geophysical Research*, *109*, A12219. https://doi.org/10.1029/2003JA010366

Fuselier, S. A., Klumpar, D. M., & Shelley, E. G. (1991). On the origins of energetic ions in the Earth's dayside magnetosheath. *Journal of Geophysical Research*, *96*, 47–56. https://doi.org/10.1029/90JA01751

Fuselier, S. A., Petrinec, S. M., & Trattner, K. J. (2000). Stability of the high-latitude reconnection site for steady northward IMF. *Geophysical Research Letters*, *27*(4), 473–476. https://doi.org/10.1029/1999GL003706

Fuselier, S. A., Trattner, K. J., & Petrinec, S. M. (2011). Antiparallel and component reconnection at the dayside magnetopause. *Journal of Geophysical Research*, *116*, A10227. https://doi.org/10.1029/2011JA016888

Gosling, J. T., Thomsen, M. F., Bame, S. J., Elphic, R. C., & Russell, C. T. (1990). Plasma flow reversals at the dayside magnetopause and the origin of asymmetric polar cap convection. *Journal of Geophysical Research*, *95*(A6), 8073–8084. https://doi.org/10.1029/JA095iA06p08073

King, J. H., & Papitashvili, N. E. (2005). Solar wind spatial scales in and comparisons of hourly Wind and ACE plasma and magnetic field data. *Journal of Geophysical Research*, *110*, A02104. https://doi.org/10.1029/2004JA010649

Lavraud, B., Dunlop, M. W., Phan, T. D., Rème, H., Bosqued, J.-M., Dandouras, I., et al. (2002). Cluster observations of the exterior cusp and its surrounding boundaries under northward IMF. *Geophysical Research Letters*, *29*(20), 1995. https://doi.org/10.1029/2002GL015464

Luo, H., Kronberg, E. A., Nykyri, K., Trattner, K. J., Daly, P. W., Chen, G. X., et al. (2017). IMF dependence of energetic oxygen and hydrogen ion distributions in the near-Earth magnetosphere. *Journal of Geophysical Research: Space Physics*, *122*, 5168–5180. https://doi.org/10.1002/2016JA023471

Mauk, B. H., Blake, J. B., Baker, D. N., Clemmons, J. H., Reeves, G. D., Spence, H. E., et al. (2016). The Energetic Particle Detector (EPD) investigation and the Energetic Ion Spectrometer (EIS) for the Magnetospheric Multiscale (MMS) mission. *Space Science Reviews*, *199*, 471–514. https://doi.org/10.1007/s11214-014-0055-5

Moore, T. W., Nykyri, K., & Dimmock, A. P. (2016). Cross-scale energy transport in space plasmas. *Nature Physics*, *12*, 1164–1169. https://doi.org/10.1038/NPHYS3869

Nykyri, K., Cargill, P. J., Lucek, E., Horbury, T. S., Balogh, A., Lavraud, B., et al. (2003). Ion cyclotron waves in the high altitude cusp: Cluster observations at varying spacecraft separations. *Geophysical Research Letters*, *30*(24), 2263. https://doi.org/10.1029/2003GL018594

Nykyri, K., Cargill, P. J., Lucek, E. A., Horbury, T. S., Lavraud, B., Balogh, A., et al. (2004). Cluster observations of magnetic field fluctuations in the high-altitude cusp. *Annales de Geophysique*, *22*, 2413–2429. https://doi.org/10.5194/angeo-22-2413-2004

Nykyri, K., Grison, B., Cargill, P. J., Lavraud, B., Lucek, E., Dandouras, I., et al. (2006). Origin of the turbulent spectra in the high-altitude cusp:Cluster spacecraft observations. *Annales de Geophysique*, *24*, 1057–1075. https://doi.org/10.5194/angeo-24-1057-2006

Nykyri, K., Otto, A., Adamson, E., Dougal, E., & Mumme, J. (2011). Cluster observations of a cusp diamagnetic cavity: Structure, size, and dynamics. *Journal of Geophysical Research*, *116*, A03228. https://doi.org/10.1029/2010JA015897

Nykyri, K., Otto, A., Adamson, E., Kronberg, E., & Daly, P. (2012). On the origin of high-energy particles in the cusp diamagnetic cavity. *Journal of Atmospheric and Solar-Terrestrial Physics*, *87*, 70–81. https://doi.org/10.1016/j.jastp.2011.08.012

Nykyri, K., Otto, A., Adamson, E., & Tjulin, A. (2011). On the origin of fluctuations in the cusp diamagnetic cavity. *Journal of Geophysical Research*, *116*, A06208. https://doi.org/10.1029/2010JA015888

Pollock, C., Moore, T., Jacques, A., Burch, J., Gliese, U., Saito, Y., et al. (2016). Fast plasma investigation for Magnetospheric Multiscale. *Space Sci. Rev.*, *199*, 331–406. https://doi.org/10.1007/s11214-016-0245-4

Powell, K. G., Roe, P. L., Linde, T. J., Gombosi, T. I., & De Zeeuw, D. L. (1999). A solution-adaptive upwind scheme for ideal magnetohydrodynamics. *Journal of Computational*, *154*, 284–309. https://doi.org/10.1006/jcph.1999.6299

Pulkkinen, T. I., Ganushkina, N. Y., Baker, D. N., Turner, N. E., Fennell, J. F., Roeder, J., et al. (2001). Ring current ion composition during solar minimum and rising solar activity: Polar/CAMMICE/MICS results. *Journal of Geophysical Research*, *106*(A9), 19,131–19,147. https://doi.org/10.1029/2000JA003036

Ridley, A. J., & Liemohn, M. W. (2002). A model-derived storm time asymmetric ring current driven electric field description. *Journal of Geophysical Research*, *107*(A8), 1151. https://doi.org/10.1029/2001JA000051

Russell, C. T., Anderson, B. J., Baumjohann, W., Bromund, K. R., Dearborn, D., Fischer, D., et al. (2016). The Magnetospheric Multiscale magnetometers. *Space Science Reviews*, *199*, 189–256. https://doi.org/10.1007/s11214-014-0057-3

Sibeck, D. G., McEntire, R. W., Lui, A. T. Y., Lopez, R. E., & Krimigis, S. M. (1987). Energetic magnetospheric ions at the dayside magnetopause—Leakage or merging. *Journal of Geophysical Research*, *92*, 12,097–12,114.

Sorathia, K. A., Merkin, V. G., Ukhorskiy, A. Y., Mauk, B. H., & Sibeck, D. G. (2017). Energetic particle loss through the magnetopause: A combined global MHD and test-particle study. *Journal of Geophysical Research: Space Physics*, *122*, 9329–9343. https://doi.org/10.1002/2017JA024268

Torbert, R. B., Russell, C. T., Magnes, W., Ergun, R. E., Lindqvist, P.-A., LeContel, O., et al. (2016). The FIELDS instrument suite on MMS: Scientific objectives, measurements, and data products. *Space Science Reviews*, *199*, 105–135. https://doi.org/10.1007/s11214-014-0109-8

Tóth, G., Sokolov, I. V., Gombosi, T. I., Chesney, D. R., Clauer, C. R., de Zeeuw, D. L., et al. (2005). Space Weather Modeling Framework: A new tool for the space science community. *Journal of Geophysical Research*, *110*, A12226. https://doi.org/10.1029/2005JA011126

Tóth, G., van der Holst, B., Sokolov, I., De Zeeuw, D., Gombosi, T., Fang, F., et al. (2012). Adaptive numerical algorithms in space weather modeling. *Journal of Computational Physics*, *231*(3), 870–903. https://doi.org/10.1016/j.jcp.2011.02.006

Trattner, K. J., Fuselier, S. A., Peterson, W. K., Chang, S.-W., Friedel, R., & Aellig, M. R. (2001). Origins of energetic ions in the cusp. *Journal of Geophysical Research*, *106*, 5967–5976. https://doi.org/10.1029/2000JA003005

Trattner, K. J., Mulcock, J. S., Petrinec, S. M., & Fuselier, S. A. (2007). Location of the reconnection line at the magnetopause during southward IMF conditions. *Geophysical Research Letters*, *34*, L03108. https://doi.org/10.1029/2006GL028397

Trattner, K. J., Petrinec, S. M., Fuselier, S. A., Nykyri, K., & Kronberg, E. (2011). Cluster observations of bow shock energetic ion transport through the magnetosheath into the cusp. *Journal of Geophysical Research*, *116*, A09207. https://doi.org/10.1029/2011JA016617

Tsyganenko, N. A. (1996). Effects of the solar wind conditions on the global magnetospheric configuration as deduced from data-based field models. In *Proceedings of the ICS-3 Conference on substorms (Versailles, France May 12-17, 1996)*, ESA SP-389, pp. 181–185.

Vontrat-Reberac, A., Bosqued, J. M., Taylor, M. G., Lavraud, B., Fontaine, D., Dunlop, M. W., et al. (2003). Cluster observations of the high-altitude cusp for northward interplanetary magnetic field: A case study. *Journal of Geophysical Research*, *108*(A9), 1346. https://doi.org/10.1029/2002JA001717

Walsh, B. M., Fritz, T. A., Klida, M. M., & Chen, J. (2010). Energetic electrons in the exterior cusp: Identifying the source. *Annales Geophysicae*, *28*, 983–992. https://doi.org/10.5194/angeo-28-983-2010

Wing, S., Newell, P. T., & Ruohoniemi, J. M. (2001). Double cusp: Model prediction and observational verification. *Journal of Geophysical Research*, *106*(A11), 25,571–25,593. https://doi.org/10.1029/2000JA000402

Wolf, R. A., Harel, M., Spiro, R. W., Voigt, G.-H., Reiff, P. H., & Chen, C.-K. (1982). Computer simulation of inner magnetospheric dynamics for the magnetic storm of July 29, 1977. *Journal of Geophysical Research*, *87*(A8), 5949–5962. https://doi.org/10.1029/JA087iA08p05949

Young, D. T., Burch, J. L., Gomez, R. G., De Los Santos, A., Miller, G. P., Wilson, P., et al. (2016). Hot plasma composition analyzer for the magnetospheric multiscale mission. *Space Science Reviews*, *199*(1), 407–470. https://doi.org/10.1007/s11214-014-0119-6

Zhang, B., Brambles, O., Lotko, W., Dunlap-Shohl, W., Smith, R., Wiltberger, M., & Lyon, J. (2013). Predicting the location of polar cusp in the Lyon-Fedder-Mobarry global magnetosphere simulation. *Journal of Geophysical Research: Space Physics*, *118*, 6327–6337. https://doi.org/10.1002/jgra.50565

Zhang, H., Fritz, T. A., Zong, Q., & Daly, P. W. (2005). Stagnant exterior cusp region as viewed by energetic electrons and ions: A statistical study using Cluster Research with Adaptive Particle Imaging Detectors (RAPID) data. *Journal of Geophysical Research*, *110*, A05211. https://doi.org/10.1029/2004JA010562